Wide-Field Optical Tracking of LEO Objects: Theoretical Assessment and Observing Strategy

Alberto Buzzoni[†]

INAF-OAS Osservatorio di Astrofisica e Scienza dello Spazio,
Via P. Gobetti 93/3, Bologna – Italy

Keywords: *Wide-field optical tracking, Astrometry, Space Surveillance and Tracking*

ABSTRACT

The main technical and strategic aspects related to Space Surveillance and Tracking (SST) with optical sensors are set in context in this study to lead to an efficient inventory of the active satellites and un-cooperant space debris population at Low-Earth orbital regimes (LEO). In particular, special emphasis is devoted to the combined interplay between timing of observations, target illumination conditions, instrumental fine tuning and data acquisition mode (surveying vs. active tracking).

At LEO altitudes, satellites are seen to cross the sky at very high angular velocity, in excess to 0.5-1.5 deg/sec, always making their positional measurements (and the inferred dynamical properties) a challenging task for ground telescopes. To this aim, objective criteria have to be identified for a best trade-off between instrument field of viev (FOV), CCD/CMOS platescale, telescope aperture and exposure time in order to maximize target(s) detection and reference grid of stars valuable for astrometry. Many counter-intuitive aspects are discussed in this regard, compared for instance with a more classical "astronomical" approach, delving in particular the widely recognized inherent link between time-tag accuracy and resolving power of optical imagery to track LEO objects.

A number of tables and graphical plots are provided for practical use to the reader.

1. Introduction

The prevailing role of private stakeholders, which from year 2017 on overcame the institutional entities in satellite and launch servicing (see, e.g., Peter 2006; Space Investment Quarterly 2017) paved the way to a pivotal change of paradigm in the access to space. Multi-satellite launches are now the rule, and mini-satellites of any kind, together with satellite mega-constellations for commercial services, pervasively populate the Low-Earth Orbital (LEO) layers around Earth (Petroni & Bianchi 2016; Lawrence et al. 2022; Kulu 2023).

Although a number of cutting-edge initiatives are under way worldwide for an active assessment of the Kessler syndrome (Kessler & Cour-Palais, 1978) through an explicit effort to "clean" space by removing debris (Liou 2011; Emanuelli et al. 2014; Newman & Williamson, 2018), yet it is recognized evidence that this approach might barely lead ever to any definitive mitigation of the problem only being realistically limited to the capture and de-orbiting of very few (4-5) dead payloads of larger size every year (e.g. Aglietti et al. 2020;

[†] Corresponding Author: Alberto Buzzoni,
email: alberto.buzzoni@inaf.it

Jankovic et al., 2020; Miller 2021; McKnight et al. 2021; Pardini & Anselmo 2021) in order to remove potentially dangerous sources of huge smaller pieces in case of hypervelocity impacts and collisions.

Indeed, in-orbit servicing and active COLA (collision avoidance) maneuvering capabilities of orbiting assets seem a more promising (but costly) solution (Stokes, 2019). And, in any case, nothing can presently be at hand to deal with possible disruptive collision/fragmentation events among fully un-cooperant debris or intact demised payloads (see e.g. Klinkrad 2006, for an exhaustive discussion).

For the latter case, and also to provide active spacecraft with the necessary space situational awareness (SSA) capabilities to implement their on-board COLA operations just in time (Peterson 2002), only a "passive" (yet proactive) space surveillance and tracking (SST) activity must be pursued from ground according to the required accuracy level in locating and characterizing the full orbiting population from the astrodynamical and physical point of view.

Radar and optical sensors can be dedicated to this aim, both providing valuable and complementary pieces of information. In particular, we know that radars can easily operate under daylight and cloudy sky, which is obviously not the case for telescopes. Radars are also smarter in assessing target velocity, via Doppler shift, but telescopes sport a superior angular resolution in locating the target on the sky and, to some extent, they can better probe target's attitude (e.g. Santoni & Piergentili 2013) and physical structure via multi-colour observations (Schildknecht et al. 2009; Hejduk, Cowardin & Stansbery 2012; Buzzoni et al. 2019). Additionally (and quite not a negligible detail), optical assets are typically one order of magnitude cheaper than radar assets, in terms of instrumental, and running costs (see, e.g. Klinkrad et al. 2008 for a few reference financial figures).

At LEO altitudes, satellite orbital path can be sampled for a large fraction (up to 10-15%) along each passage over the same ground location; this means that accurate astrometry along such a large arc across the sky with wide-field sensors greatly helps constrain, in principle, orbital parameters in almost real-time. Timeliness is the crucial requirement when assessing LEO traffic as orbits tend to quickly evolve under the influence of gravity perturbation especially due to Earth oblateness and to the residual atmospheric drag, which still plays a role up to 600-1000 km altitudes.

In this paper we want to make an up-to-date appraisal of SST strategies for the dynamical characterization of the LEO population including a comparative discussion of the distinctive and complementary contribution of surveying vs. tracking operational approach. After reviewing in Sec. 2 some relevant characteristic of LEO dynamics, in particular the implied timescales for ground visibility according to satellite altitude, our assessment is argumented in Sec. 3, with special attention to the ancillary constraints dealing with satellite shadowing conditions and optimal time window(s) for ground observations with changing geographical latitude and yearly season (Sec. 3.1).

The required instrumental performance for optical telescopes is also investigated in the same Section (Sec. 3.2), especially in terms of detector platescale (PS) and field of view (FOV) covered on sky. Both these figures strictly relate with the telescope ultimate efficiency in target detection and positional measurements in case of fast-moving celestial objects (Sec. 3.3 and 3.4).

Astrometry and time tag are the two parallel domains that we should properly tackle for an optimum constraint of the orbiting targets (Sec. 3.5). At the ISS altitude (say 400 km), an astrometric accuracy of 1 arcsec leads to confine the target position within 2 meters transverse to the motion direction, while for the same figure to be reached along the motion vector, a far more challenging time lapse of just 0.25 millisec must be appreciated to tag our observation.

Our results are finally discussed and summarized in Sec. 4, and an essential excerpt of the "Three Golden Rules" for an optimum optical tracking of LEO objects concludes, in Sec. 5, our brief review. A number of tables and graphical plots will accompany our discussion along the different sections, especially intended for practical use.

2. Assessing LEO dynamics

According to Kepler's Third Law, an object in (circular) orbit around Earth appears to move to any external observer in an inertial frame with angular velocity,

$$\omega = \left[\left(\frac{GM_E}{R_E^{\ 3}} \right)^{1/2} \frac{1}{(1+q')^{3/2}} \right] \approx \frac{0.071}{(1+q')^{3/2}} \quad \text{deg/s} \tag{1}$$

providing to express satellite's altitude q' in unit of Earth radius, $R_E = 6378km$, and recalling the Earth mass $M_E = 5.97 \times 10^{24}\, kg$ and the gravitational constant $G = 6.67 \times 10^{-11}$ in Si units. As Earth itself rotates, at its own angular velocity $\omega_E = 360^o / 86400s \approx 0.0042^\circ \text{s}^{-1}$, for a geocentric observer, the satellite's apparent angular speed will either be $\omega_{sat} = \omega - \omega_E$ for a prograde orbit (i.e. $i < 90^o$) or $\omega_{sat} = \omega + \omega_E$ for a retrograde orbit ($i > 90^o$).

In addition, for an observer on Earth's surface (evidently closer to the target from its own observing point), the apparent angular velocity will be further increased by a factor $(1+q')/q'$ so that, in case of a zenith passage, a satellite at height q' is seen to move angularly at a rate ω_{sat} equal to:

$$\omega_{sat} \approx \left[\frac{1}{14.1\ (1+q')^{3/2}} \mu \frac{1}{240} \right] \frac{1+q'}{q'} \quad \text{deg/s}, \tag{2}$$

where the minus sign in the second term within brackets applies to prograde orbits and the plus sign to retrograde ones. As at LEO regimes, the term for ω_E is negligible, a useful approximation of eq. (2) becomes:

$$\omega_{LEO} \approx \frac{0.071}{q'(1+q')^{1/2}} \quad \text{deg/s} \tag{3}$$

Accordingly, the (sideral) period (P_{sat}) of the body's revolution around Earth simply derives from eq. (1) as $\omega = 360^o / P_{sat}$, namely

$$P_{sat} \approx 84.6\ (1+q')^{3/2} \ \text{min}, \tag{4}$$

which is typically in the range 90-106 minutes for satellites lower than ~1000 km in quote.

Table 1 - Apparent zenith angular velocity and visibility horizon for objects in LEO orbit

Altitude [km]	q'	Visibility horizon [km]	ω_{sat} [deg/sec]		Altitude [km]	q'	Visibility horizon [km]	ω_{sat} [deg/sec]	
			prograde	retrograde				prograde	retrograde
200	0.031	3154	2.09	2.37	650	0.102	5529	0.62	0.71
250	0.039	3515	1.67	1.89	700	0.110	5721	0.57	0.66
300	0.047	3838	1.38	1.57	750	0.118	5904	0.53	0.61
350	0.055	4133	1.18	1.34	800	0.125	6080	0.50	0.57
400	0.063	4404	1.03	1.17	850	0.133	6249	0.47	0.54
450	0.071	4657	0.91	1.04	900	0.141	6411	0.44	0.50
500	0.078	4894	0.81	0.93	950	0.149	6568	0.41	0.48
550	0.086	5117	0.74	0.84	1000	0.157	6719	0.39	0.45
600	0.094	5328	0.67	0.77					

In **Fig. 1** and **Tab. 1** we report the values of ω_{sat} from eq. (2) for objects in orbit at various LEO altitudes. One sees from the figure that at LEO regimes a satellite crosses the sky typically at about 0.5°-1.5° s^{-1}. Due to the effects of perspective and the increased distance (slant range) of the satellite, the apparent angular velocity tends to slow down with increasing the zenith angle ζ and it scales approximately as the inverse of the astronomical air mass. Therefore, in general, we have that

$$\omega_{sat}(\zeta) \approx \omega_{sat}(0)/\sec(\zeta) . \tag{5}$$

It should be noted that as ζ increases, the effect of a larger latency time of the target on the detector pixel exactly compensates for the increased distance; however, as the incoming flux scales down with the square of the distance, we always have a net loss of efficiency when observing objects as they lowers towards the horizon.

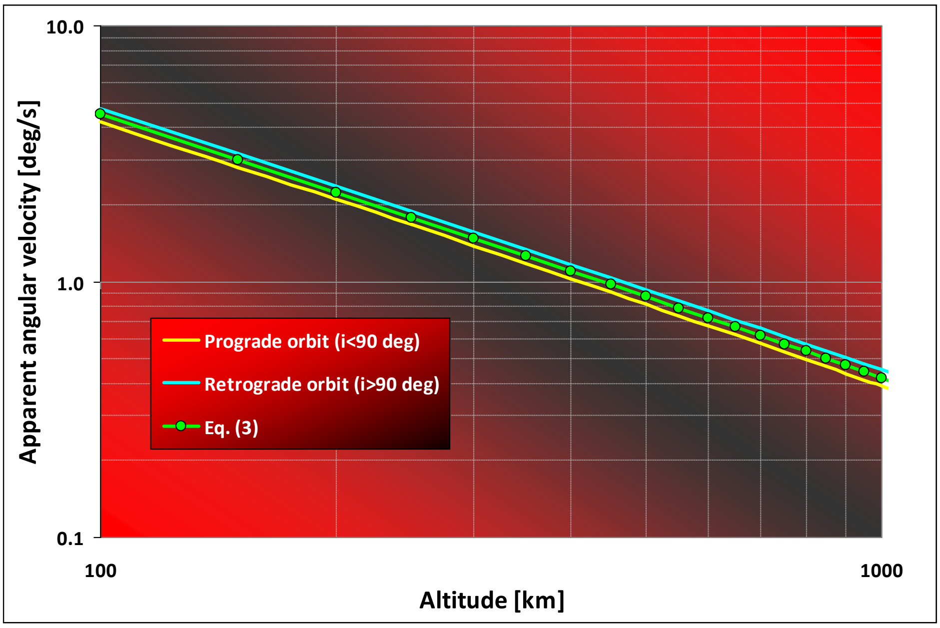

Figure 1 - Apparent angular velocity, as seen from a ground observing station, for objects in prograde (yellow curve) and retrograde (cyan curve) orbit, at high elevation above the horizon, as in eq. (2). The approximate relationship as from eq. (3) is also displayed (green points and curve).

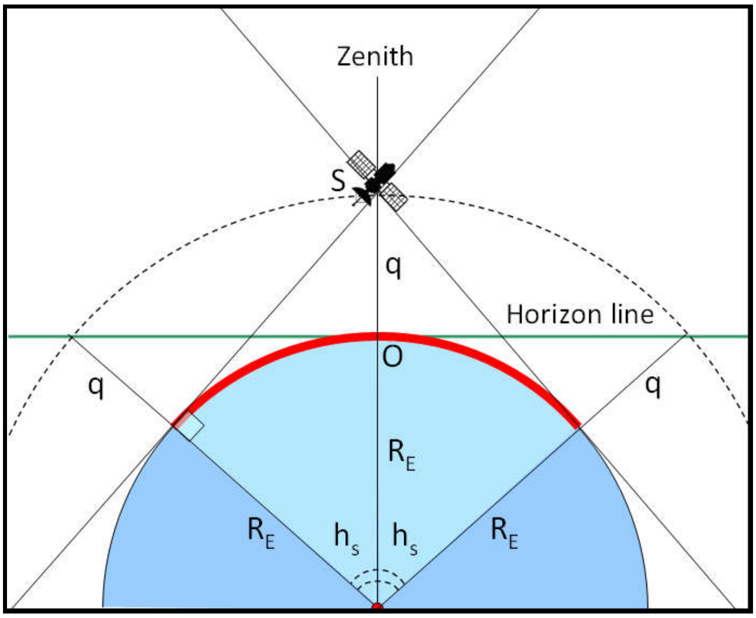

Figure 2 – The geometric reference for the visibility horizon (red arc) from a satellite orbiting at an altitude "q".

The geometric circumstances for object visibility, in case of a zenith passage, are a classical problem (see f.i. Macko 1962) and can be assessed with the help of **Fig. 2**.

In order to evaluate the angle h_s, one has to recall the Law of Sines for triangles so that $\frac{R_E}{\sin(180^o - 90^o - h_s)} = \frac{R_E + q}{\sin(90^o)}$, or $\frac{R_E}{\cos(h_s)} = \frac{R_E(1+q')}{1}$. Then,

$$h_s = \arccos\left[\frac{1}{1+q'}\right]. \tag{6}$$

Under many respects, the angle h_s is a meaningful parameter for our analysis as

1) it gives the Sun's (negative) elevation for Earth's shadow terminator to cross at the zenith at quote q;
2) the arc $2R_Eh_s$ (by expressing h_s in radians) gives the portion of Earth which the satellite is in sight from or, equivalently, the Earth's subtended horizon as reached from the satellite point of view;
3) the quantity $2(R_E + q)h_s$ is the maximum length of satellite's visibility arc from a ground-based observer "O";
4) finally, the ratio (h_s / π) provides the maximum fraction of satellite's orbit potentially sampled in a passage by a ground-based observer. As we mentioned before, for LEO altitudes this fraction turns to be around 10-15%.

Figure 3 reports the satellite visibility horizon with increasing object's altitude. As expected, note from the figure that a maximum arc length $\pi R_E \approx 20{,}037$ km (namely the Earth's whole hemisphere cap) is reached asymptotically for the farthest satellite lookouts.

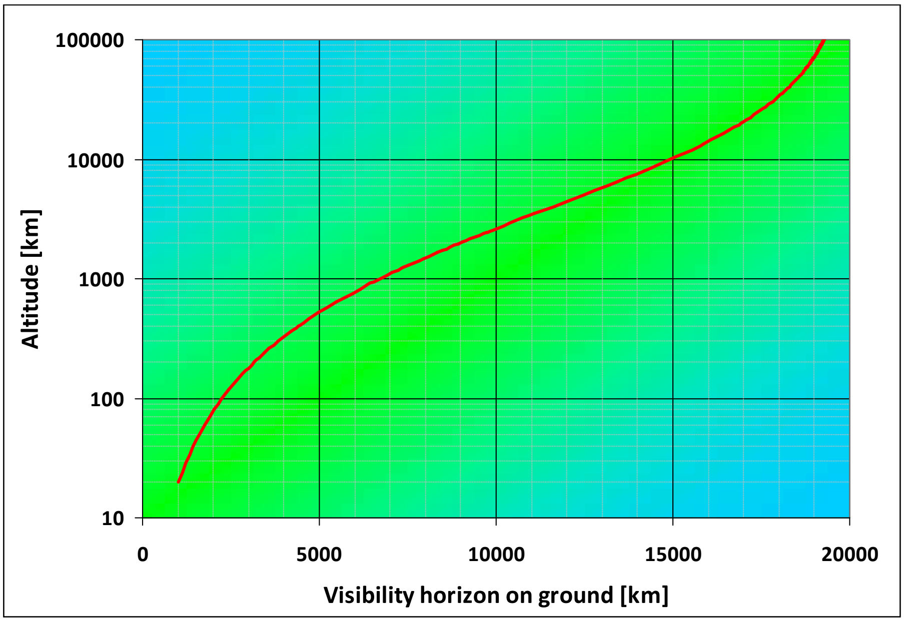

Figure 3 – The satellite visibility horizon for orbits at different altitude. Note that the horizon tends asymptotically to the whole hemisphere πR_E ~20,000 km when the satellite moves very far away from Earth.

3 Observing strategy

For actual optical tracking, LEO objects require to be sunlit, that is off the Earth's shadow cone. At such low altitudes, however, this is a quite severe condition which restrains observations to only a tight window, every night, just after the sunset or just before the dawn (see e.g., Hainaut & Williams 2020, and Lawler, Boley & Rein 2022 for a thoughtful analysis).

3.1 Timing and shadowing conditions

At the beginning of night, the nautical twilight sets the natural reference condition to start SST observations. By definition, this requires the Sun to be 12^o below the horizon, which makes stars to appear at naked eye. The nautical twilight depends on Sun's declination (i.e. the yearly season) and on observer's latitude. It relies on the standard relationship (e.g. Meeus 1991) to set the Sun hour angle H:

$$H = \arccos\left[\frac{\sin(\varepsilon) - \sin(\lambda)\sin(\delta)}{\cos(\lambda)\cos(\delta)}\right], \qquad (7)$$

where δ is the Sun's declination, ε is the Sun's elevation angle (negative for our scope), and λ is the observer's latitude. By assessing eq. (7) for $\varepsilon = 0^o$ and $\varepsilon = -12^o$ we easily obtain the timing from the local sunset suitable to start SST observations[1]. Providing to express $H(\varepsilon)$ in degrees, this lapse (in minutes) is $t_{\rm naut} = 4(H_{-12} - H_0)$. Similarly, for $\varepsilon = -18^o$, eq. (7) sets the astronomical twilight, at which sky is dark enough to start standard astronomical observations. Again, $t_{\rm astro} = 4(H_{-18} - H_0)$ gives the corresponding time lapse (in minutes) from the sunset.

[1] A more strict treatment of the sunset problem requires to set $\varepsilon = -0.83^o$ and also consider the atmosphere refraction (see, e.g. Montenbruck & Pfleger 1994). The net effect however is negligible and for the scope of our discussion it is amply sufficient to set $\varepsilon = 0^o$ for the horizon crossing time.

Table 2 – Nautical and Astronomical Twilight instants, in minutes after the local sunset (or before the dawn) for an observer located at the equator (λ= 0°) or at mid-latitude in the Northern (λ= 45°) and Southern (λ= -45°) hemisphere.

Date	Nautical Twilight			Astronomical Twilight		
	λ= -45°	λ= 0°	λ= 45°	λ= -45°	λ= 0°	λ= 45°
1-Jan	92	52	76	156	79	112
15-Jan	88	52	75	145	77	110
1-Feb	81	50	72	129	76	106
15-Feb	75	49	70	118	74	104
1-Mar	71	48	68	110	73	102
15-Mar	69	48	68	105	72	103
1-Apr	68	48	70	102	72	106
15-Apr	69	49	72	103	73	112
1-May	70	50	77	105	75	122
15-May	73	51	83	107	76	133
1-Jun	75	52	89	111	78	149
15-Jun	77	52	93	112	79	158
1-Jul	77	52	92	112	79	157
15-Jul	75	52	88	110	78	147
1-Aug	72	51	82	107	76	131
15-Aug	70	50	77	104	74	120
1-Sep	68	49	72	102	73	111
15-Sep	68	48	69	103	72	106
1-Oct	69	48	68	105	72	103
15-Oct	72	49	68	110	73	102
1-Nov	77	50	70	120	74	104
15-Nov	82	51	72	132	76	107
1-Dec	89	52	75	147	78	110
15-Dec	92	52	77	157	79	112

Table 2 reports the relevant time stamps for nautical and astronomical twilight instants in minutes after the local sunset (or, equivalently, before the dawn), along the year, for an observer located at the equator and at mid-latitude in the Northern and Southern hemisphere. Accordingly, the reference timing for SST activities along the year, is shown in **Fig. 4**; at the beginning of night, observations are allowed yet 50±2 minutes after the sunset from the Equator and 80±12 minutes from λ= ±45°.

As far as the night proceeds and the Sun lowers below the horizon, the incoming Earth's shadow begins to raise from the Eastern horizon preventing LEO objects to be detected optically. The exact geometrical circumstances for satellite shadowing can now be assessed with the help of **Fig. 5** (see also Hainaut & Williams 2020 for a complementary treatment).

In particular, the two triangles $T\hat{S}C$ and $C\hat{S}O$ in the figure, sharing the satellite vertex, give us the relevant references for our analysis.[2]

[2] The Earth shadow under Sun's illumination is actually a cone with its apex located at a geocentric distance z. A straightforward geometrical proportion relates z with the radius of the shadow cone S_q at a given quote q' above Earth's surface, namely $R_S:(Z+z)=R_E:z=S_q:[z-R_E(1+q')]$, where R_S is

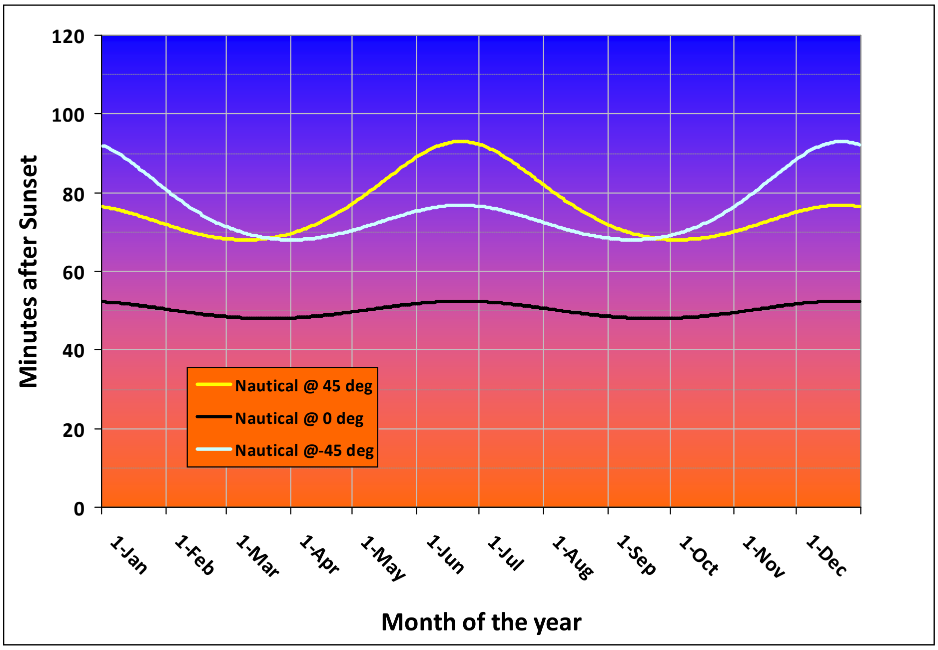

Figure 4 - The Nautical Twilight circumstance, in minutes after the local sunset (or before the dawn) for an observer located at the equator (black line) or at mid-latitude in the Northern (yellow line) and Southern (cyan line) hemisphere. The Nautical Twilight instant may set the start of SST optical observations.

Under an assumed timing and the corresponding Sun's elevation angle h_s, in the figure, a ground observer "O" looks at a satellite "S", crossing the shadow terminator at a zenith angle ζ (or, equivalently, at an elevation angle $\varepsilon = 90^o - \zeta$). The geocentric angle β can be taken as a running parameter in our scenario to constrain both the azimuth angle and the location of the terminator line with the quote.

By applying the Law of Sines to the triangle $C\hat{S}O$, we set $\frac{R_E + q}{\sin(180^o - \zeta)} = \frac{R_E}{\sin(\varphi_2)}$, which leads to $\frac{(1+q')}{\sin(\zeta)} = \frac{1}{\sin[(180^o - \beta) - (180^o - \zeta)]}$, or $\frac{1}{1+q'} = \frac{\sin(\zeta)\cos(\beta) - \cos(\zeta)\sin(\beta)}{\sin(\zeta)}$.

On the other hand, in force of eq. (6), by relying on the triangle $T\hat{S}C$, the quote q that fulfills the geometrical shadowing condition requires, in general, that $(R_E + q)\cos(h_s - \beta) = R_E$. By combining the two pieces of information, the final relationship between ζ and q' can be obtained in parametric form via the angle β, as

the Sun's radius and Z is the Sun-Earth distance. From the first two terms of the proportion (and recalling that $R_S >> R_E$) we have that $(R_E/z) \approx 1/213$; on the other hand, by combining the second and third term, we obtain, with little arithmetic: $(S_q/R_E) = [1 - (1+q')/213]$. This leads to estimate, for instance, that at a quote of, say, 1000 km, the radius of the shadow cone is just 0.5% or ~35 km smaller than the Earth physical radius, a difference that reflects in just a few seconds in satellites illumination/shadowing circumstances. To all practical extent, for our discussion in the LEO context, we therefore can safely consider Earth's shadow as a cylinder extending opposite to the Sun's direction.

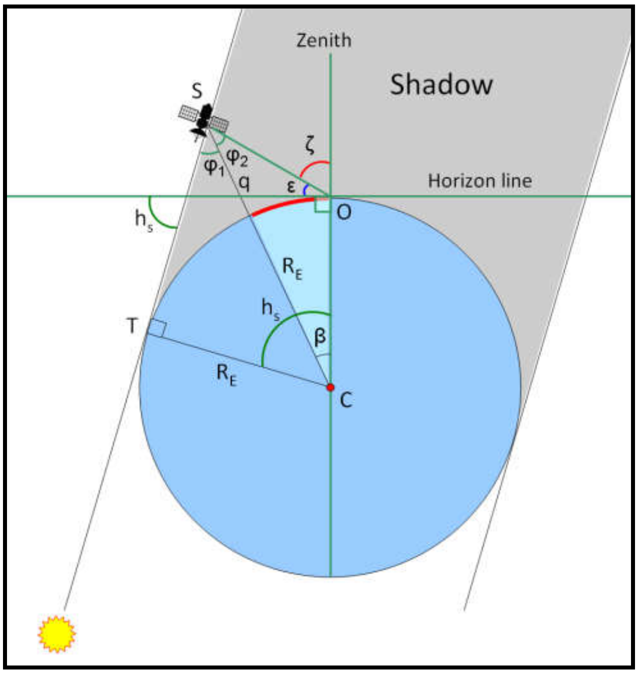

Figure 5 – The geometric reference for the shadowing conditions of a satellite "S" orbiting at an altitude "q", as seen from an observer "O" at a zenith angle ζ .

$$\left\{ \begin{aligned} 1+q' &= \frac{1}{\cos(h_s-\beta)} \\ \tan(\zeta) &= \frac{\sin(\beta)}{\cos(\beta)-\cos(h_s-\beta)} \end{aligned} \right\}, \ \forall \beta \in [-h_s, +h_s]. \tag{8}$$

Note that eq. (8) are nominally independent from the observer's location and yearly season; they can be applied to any suitable geographic situation and timing by simply converting the Sun's elevation angle h_s into an appropriate hour angle, through eq. (7).

Two illustrative scenarios are displayed in the panels of **Fig. 6**, respectively for an observer at the Equator and at (Northern) mid-latitude, around the solstice seasons, that is for $\delta \approx 0$ in eq. (7). Taking into account also for the nautical twilight timing, at mid latitude it is evident from the figure that LEO objects below 1000 km can be efficiently tracked with optical telescopes within a time window of some 100±12 minutes after the sunset (or before the dawn) by counting on at least half a sky vault (face West at sunset and face East at dawn) sunlit. The favourable window shrinks to a mere 70±2 min when observing from the Equator.

3.2 Tracking vs. surveying

Kine-theodolite batteries are iconic heritages of the early years of the space era (Veis, 1963; see as well King-Heele 1983 for an evocative technical recount of those years) when these instruments were extensively used to track the first Russian and American satellites along their path around Earth. The strategy aimed at docking the target and following it up along a portion of its trajectory with repeated positional measurements in order to reconstruct and/or refine the orbit. The tracking strategy requires in general a demanding technical effort from the mechanical point of view, especially for big (heavy) telescopes or radar antennas, facing the severe inertial constraints of the mounting hardware.

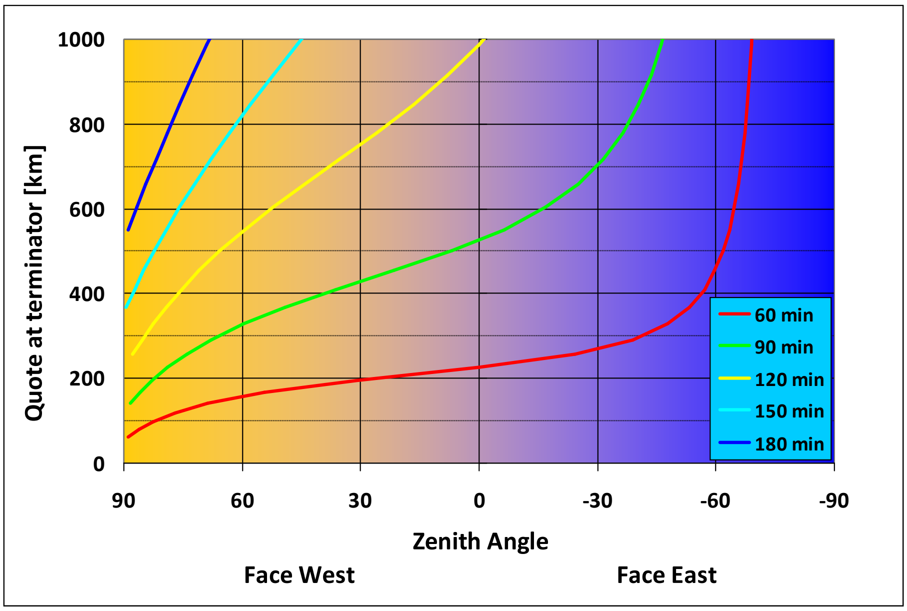

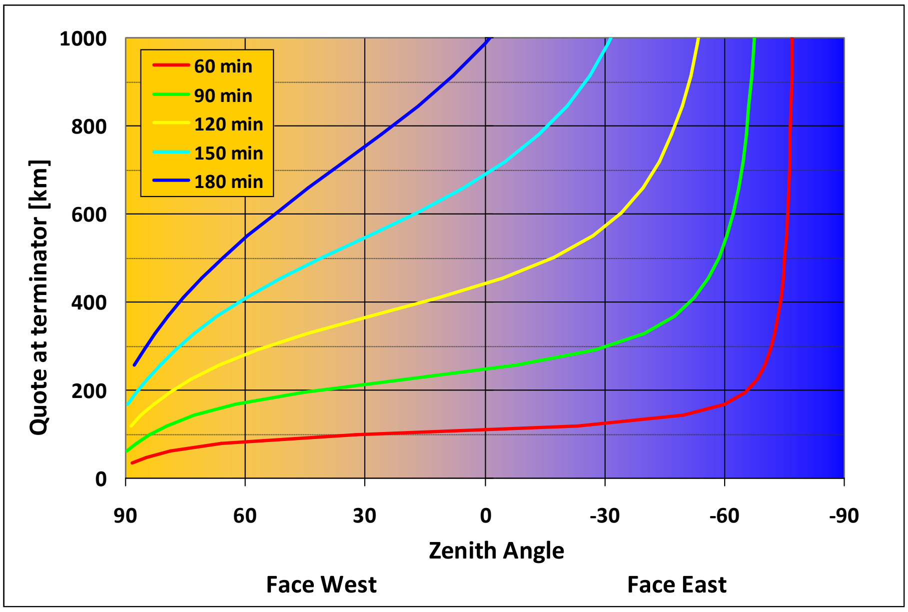

Figure 6 – The quote and zenith angle of Earth's shadow terminator along the night for two observers located at the Equator (upper panel) and at λ= 45° (lower panel) around the solstice seasons (i.e. Mar-Apr and Sep-Oct). The relevant relationship is given for different time delays in minutes *after* the local sunset (or *before* the local dawn), by matching eq. (8) and (7), as displayed in the inset legend. Orbiting objects are sunlit only left to each curve. For the beginning of night, zenith-angle notation assumes positive values when looking West and negative values "face East". The opposite is true for the dawn observations.

More prudently, one may choose instead to "stare and wait", making the telescope ready to catch the target as soon as (and if) it shows up at some point. Compared to the active tracking, the surveying strategy tends to simply shift the operational challenge from mechanics to optics as we ideally need our sensor to span a FOV as wide as possible (ideally, by matching the entire field of regard, FOR) to maximize the observing chance and avoid (or minimize) any pointing maneuvering. In addition, as we have to manage exposure sequences on milliseconds timescales, any detector with electronic reading instead of mechanical shutter should nowadays be preferred. CMOS, in their different technical flavours, are the elective devices, all the way (Schildknecht et al. 2013; Cooper et al. 2019).

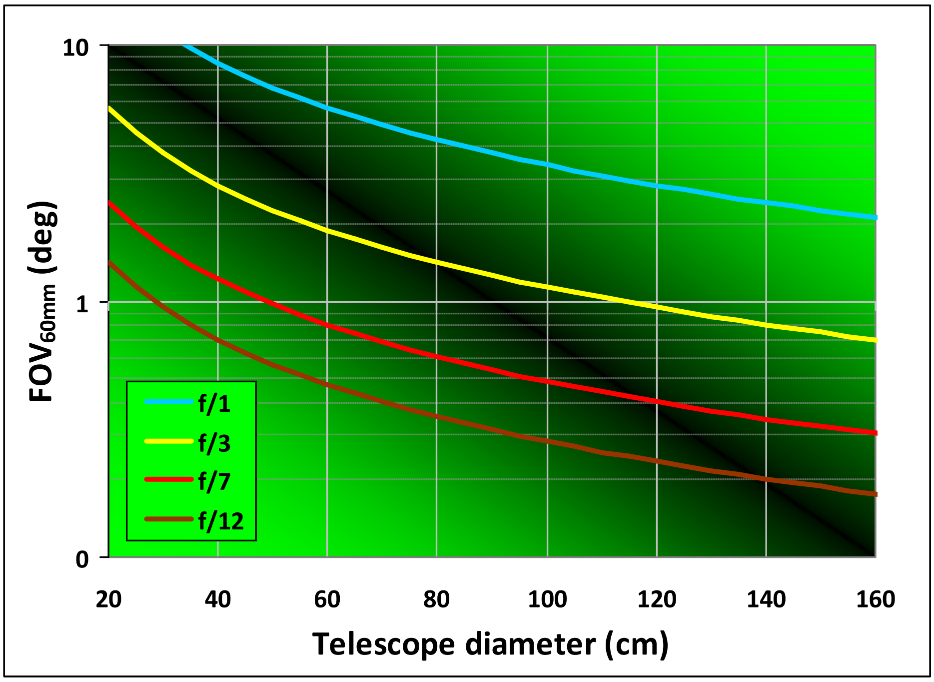

Figure 7 – The projected FOV on a Medium Format (60x60 mm) CMOS, for telescopes of different size and relative aperture (f-number).

Both for telescopes and radio antennas, an increasingly wider FOV requires an overwelmingly compact sensor, sporting a "fast" relative aperture, the so-called "f/number", $f = F/D$, that is the focal length (F) must be as short as possible relative to sensor aperture (D). Just restraining our analysis to optical telescopes (but fully similar arguments hold for radars, as well), the expected platescale (PS) at the focus of the instrument can be estimated as

$$PS \sim \frac{206}{fD} \text{ arcsec/mm,} \tag{9}$$

providing to express the telescope diameter in meters. The platescale directly constrains the projected FOV on the sky and the physical size of the spotted image at the telescope focus, to be (totally or partially) intercepted by one or more detector(s). As current micro-chip technology still prevents COTS detectors to exceed the commercial Medium Format size[3] (i.e. 60 x 60 mm) then, in terms of covered FOV, one single chip of Σ mm on a side is worth

$$FOV \leq \left(\frac{3.4}{fD}\right)\left(\frac{\Sigma_{mm}}{60}\right) \text{ deg.} \tag{10}$$

Figure 7 gives a summary of the different technical scenarios according to the formula. Note from the figure that a wide field in excess to 1° with good sensitivity, as in metric-class telescopes, always requires challenging f-numbers, $f \leq 3$. More standard optical designs (f/7 or higher) may be in the order, but at cost of falling back to smaller telescopes of decimetric class.

[3] Current advances in chip technology push in the direction of decreasing the pixel size in order to maximize image resolution rather than increasing the chip size for a larger FOV.

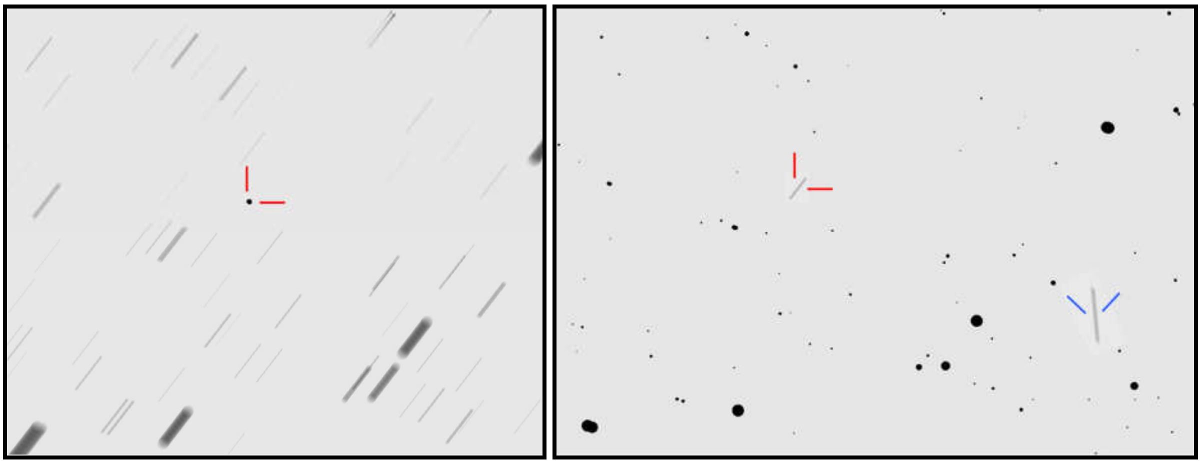

Figure 8 – An illustrative sketch of the tracking (left panel) vs. surveying (right panel) strategy. Shallower stars and an enhanced target signal (red markers) is secured by docking the object, like in the left panel. However, as stars trail across the field, most of them (all those which totally or partially overspill del FOV borders) end up to be useless for any astrometric calibration. In addition, by focussing on the envisaged target, the tracking telescope looses a serendipitous intruder (trailing in the right panel and marked in blue) which, on the contrary, is caught by the surveying sensor.

FOVs in excess to these limits can obviously be attained under very special observing circumstances. This is the case for instance of dedicated astronomical surveys with big telescopes, by relying on mosaicing or dithering techniques, although this is known to drastically magnify costs and require an important added value on the side of data-flow management and of more elaborated image reduction procedures.

As shown in **Fig. 8**, overall, a number of favorable conditions generally benefit the "surveying" over "tracking" strategy, as

- A tracking telescope can only focus on one specific target at a time while a surveying sensor normally takes advantage of a better SSA capabilities and may easily include additional or intervening serendipitous targets;
- With a tracking telescope we better follow up a target with reasonably known preliminary orbit. Any extemporary deviation from the expected scheme, due for instance to in-orbit maneuvering or intervening dynamical perturbations (e.g. atmosphere drag etc.) is difficult to be properly assessed from the observing point of view. This is not a problem for a surveying strategy;
- The target positional information requires a suitable grid of surrounding calibration stars. If we dock the target, stars appear as trailing objects. The opposite occurs for the surveying strategy where a trailing target is surrounded by a plot of "fixed" stars. Whatever, either target or star trails must be fully comprised within the FOV to be useful for astrometry (see, again the illustrative case of **Fig. 8**). As a result, even in tracking mode, exposure time (and the inherent target S/N detection threshold) always has to be maintained short enough for star trails not to overspill the FOV borders. According to the target apparent angular velocity (ω_{sat}), the maximum exposure time allowed for tracking across a given FOV easily derives from eq. (10) as

$$\tau_{\max} \leq \left(\frac{3.4}{\omega_{\text{sat}}\,\text{fD}_{\text{m}}}\right)\left(\frac{\Sigma_{mm}}{60}\right) \quad \text{sec}, \tag{11}$$

with ω_{sat} in deg/sec, Σ in mm and D in meters. Under any realistic condition, one sees from the equation that a few seconds can be spent at most to track a LEO target in one single shot.

3.3 Magnitude limit

When surveying fast-moving satellites we must properly deal with their latency time, τ_{px}, that is the lapse spent by the object on one single pixel of the CMOS detector. By recalling eq. (9), with the appropriate unit transformation and expressing the pixel size (px_μ) in µm, the telescope diameter in meters and the satellite angular velocity (ω_{sat}) in deg/s, we have

$$\tau_{px} = \frac{57}{\omega_{sat}} \frac{\mathrm{px}_\mu}{fD_m} \quad \mu\mathrm{s} \tag{12}$$

with latency expressed in microsenconds. Ideally, this is the maximum useful time for the pixel to collect the signal. Paradoxically, any longer exposure will eventually worsen target detection, in terms of signal to noise ratio, $(S/N)_{sat}$, depending the number of pixels (n_{px}) the signal is spread on. For an exposure of $\tau_{\exp}$ seconds, we evidently have $n_{px} = \tau_{\exp}/\tau_{px}$ so that

$$(\mathrm{S/N})_{\mathrm{sat}} = \frac{\mathrm{S/N}(\tau_{px})}{\sqrt{n_{px}}} = \mathrm{S/N}(\tau_{px})\sqrt{\frac{\tau_{px}}{\tau_{\exp}}} \tag{13}$$

that is, $(\mathrm{S/N})_{sat} \propto \tau_{\exp}^{-1/2}$ (Buzzoni et al. 2016). Conversely, in the case of active sideral tracking, like for instance in any standard astronomical context, a star will come detected with increasing clarity as exposure time increases, being in this case $(\mathrm{S/N})_* \propto \tau_{\exp}^{1/2}$. Therefore in the context of SST surveying operations, the effect of an increased exposure time leads to a shallower contrast of the target compared to the surrounding star field. *Actually, the larger the track across the field the vanishing the target appears with respect to an increasingly sharper surrounding star field.The opposite occurs in case of active tracking* with a target that now sharply emerges $[(\mathrm{S/N})_{sat} \propto \tau_{\exp}^{1/2}]$ with respect to the shallowing plot of surrounding trailing stars $[(\mathrm{S/N})_* \propto \tau_{\exp}^{-1/2}]$ with increasing image integration[4].

By recalling the basic definitions, in terms of magnitude limit reached at fixed S/N detection level, for trailing objects we can therefore identify two trends by comparing with the latency timescale:

$$\begin{cases} \mathrm{Mag}_{\mathrm{lim}} = 1.25 \cdot \log \tau_{\exp} + \mathrm{const} & \text{if } \tau_{\exp} \le \tau_{px} \\ \mathrm{Mag}_{\mathrm{lim}} = -1.25 \cdot \log \tau_{\exp} + \mathrm{const} & \text{if } \tau_{\exp} > \tau_{px} \end{cases} \tag{14}$$

The equation set show that as long as an object (either target or star) can be maintained as a point source on the detector, then increasingly fainter magnitudes can be reached with increasing the exposure time. On the contrary, if it is let trailing across the field in excess to its characteristic latency time (set by the apparent angular motion for a satellite, or the

---

[4] But see the limit set by eq. (11), as discussed in previous section.

sideral rate for a star), then the corresponding signal becomes more and more "diluted" making the object to vanish amid the noise with increasing $\tau_{\exp}$.

For LEO satellites, the latency time increases with the orbital altitude and, by virtue of eq. (3), it scales as $\tau_{px} \propto q'^{3/2}$. On the other hand, the larger distance makes the apparent flux to fade in reason of $\lambda_{sat} \propto q'^{-2}$ so that the net effect of satellite quote on detection efficiency is that $S/N(\tau_{px}) \propto (\tau_{px} \times \lambda_{sat}) \propto q'^{-1/2}$.

3.4 Astrometry and positional uncertainty

Photometric properties of SST observations directly influence the astrometric performance of our positional measurements, while constraining the orbit of the observed targets. In general, the astrometric solution requires a suitable grid of reference stars to surround the target down to a magnitude limit which must be deeper the smaller the sampled FOV of our observations.

Providing the target photometric barycenter to be located across the field within a standard deviation σ_{obs}, and assuming to calibrate this nominal position by means of a grid of "n_*" reference stars, each with its inherent positional uncertainty σ_{cat}, then a total variance σ^2_{sat} for the target astrometry can be estimated as

$$\sigma^2_{sat} = \sigma^2_{obs} + \frac{\sigma^2_{cat}}{n_*} \tag{15}$$

A trade-off is therefore mandatory to set the optimum exposure time in order to keep it as short as possible to minimize the "internal" error σ_{obs} and "freeze" the relevant target position, but large enough to have a suitable number of surrounding reference stars with good S/N such as to reduce the "external" error component induced by σ_{cat}.

One supplementary reason that calls for the exposure time to ideally approach τ_{px} is that photometric barycenter may be affected by the target variability, especially for tumbling space debris or demised spacecraft. This is by far the prevailing source of internal uncertainty in case of trailing objects (Buzzoni et al. 2019) as it makes difficult any exact "cut" of the satellite track over the background. The only way to overcome or mitigate the effect is evidently to restrain the integration time to a prudent fraction of the variability timescale, then in a range of some tenths of second or so.

The target positional information on the chip must eventually be converted into absolute celestial coordinates via comparison with a calibration grid of surrounding reference stars. According to eq. (15), both the inherent accuracy of the star catalog (σ_{cat}) and the number of available stars in our FOV set the ultimate performance of our measure. As summarized in **Tab. 3**, the catalog accuracy has been dramatically improving in the recent years, smashing the milliarcsec threshold in the astrometry measurements with the Gaia's overwhelming database.

Table 3 – Positional uncertainties of different reference star catalogs for astrometric applications

Catalog	σ_{cat} [mas]	Reference
Tycho-2	7-60	Høg et al. (2000)
GSC-II	200-280	Lasker et al (2008)
PPMXL	80-300	Roeser S., Demleitner M., Schilbach E. (2010)
CMC-15	50-100	Niels Bohr Inst. (2014)
URAT-1	5-40	Zacharias N., et al. (2015)
UCAC-5	10-70	Zacharias N., Finch C., Frouard J. (2017)
Gaia DR2	0.02-0.50	Lindegren et al. (2018)
Gaia DR3	0.01-0.10	Gaia collaboration (2023)

In their seminal study on the Galaxy dynamics, Bahcall and Soneira (1980) provided a useful analytical model to estimate the star count density at various apparent magnitudes and at different Galactic coordinates. In the most conservative hypothesis of our interest, i.e. by sampling the star field at latitudes around the North Galactic Pole (b = 90^{o}) we obtain the cumulative number of stars as in **Tab. 4** and **Fig. 9**. As some ten stars per square degree seem a good figure for accurate astrometry, then we need to reach V~12 with our observations. Star density drastically increases, of course, over one order of magnitude when moving toward the Galaxy plane (see, e.g. Allen 1973) so that shallower imagery (i.e. shorter exposure times) are allowed (and recommended) when looking at the Milky Way equatorial direction.

With some caution, experience indicates that good astrometry usually matches a fraction (1/5-1/7) of pixel, that is well less than one arcsec, depending on the detector platescale. This leads to uncertainties of a few meters for target location "transverse" to the motion vector at LEO.

Table 4 – Cumulative star counts per square degree, with increasing apparent V magnitude, at the North Galactic Pole according to the Bahcall & Soneira (1980) model

Apparent magnitude V	No. of stars/sq. deg	One star every [deg]	Apparent magnitude V	No. of stars/sq. deg	One star every [deg]
6.0	0.051	4.45	13.5	34	0.17
6.5	0.081	3.51	14.0	49	0.14
7.0	0.13	2.77	14.5	70	0.12
7.5	0.21	2.19	15.0	98	0.10
8.0	0.33	1.74	15.5	137	0.09
8.5	0.52	1.38	16.0	188	0.07
9.0	0.82	1.10	16.5	255	0.06
9.5	1.3	0.88	17.0	342	0.05
10.0	2.0	0.71	17.5	452	0.05
10.5	3.1	0.57	18.0	588	0.04
11.0	4.7	0.46	18.5	753	0.04
11.5	7.1	0.38	19.0	949	0.03
12.0	11	0.31	19.5	1178	0.03
12.5	16	0.25	20.0	1440	0.03
13.0	23	0.21			

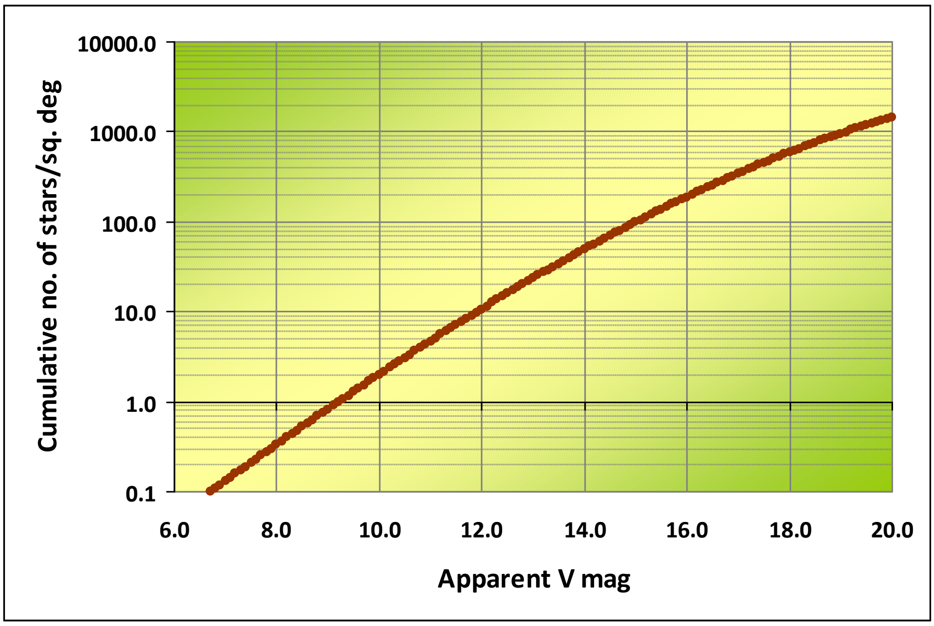

Figure 9 – Cumulative star counts per square degree, with increasing apparent V magnitude, at the North Galactic Pole according to the Bahcall & Soneira (1980) model.

3.5 Clock fine-tuning and error budget

According to previous figures, orbital assessment of fast-moving targets in LEO requires for our observations to confidently constrain position in the space-time domain at a time. To some extent, this approach largely differs from the standard astronomical observations as dynamics of Earth orbiting objects proceeds on far shorter timescales compared to celestial events due to the important absolute velocities (i.e. some 8 km/s) involved in LEO traffic and the relatively close distance from us (i.e. <1000 km or so).

A fine tuning of the clock is therefore at least as important as a thorough astrometric assessment of the target. This concept is illustrated in **Fig. 10** where we contrast the required accuracy of astrometry and time-tag to reach the same absolute metric accuracy in orbit colocation at the different LEO altitudes.

In fact, as we have been discussing in previous section, while good astrometry usually constrains target location "transverse" to the motion vector within a few meters uncertainty, a similar accuracy along the motion direction would imply a clock accuracy on a millisecond timescale, far a more challenging technical performance in terms of telescope exposure management.

The tight space-time connection is of immediate relevance as far as the satellite angular rate is assessed from the telescope imagery to therefrom infer the period and the semi-major axis of the orbit. If an arclet of angular length S is sampled in a time τ for a satellite pass, then

$$\omega_{sat}\tau = 2\pi\frac{\tau}{P} = S\,. \qquad (16)$$

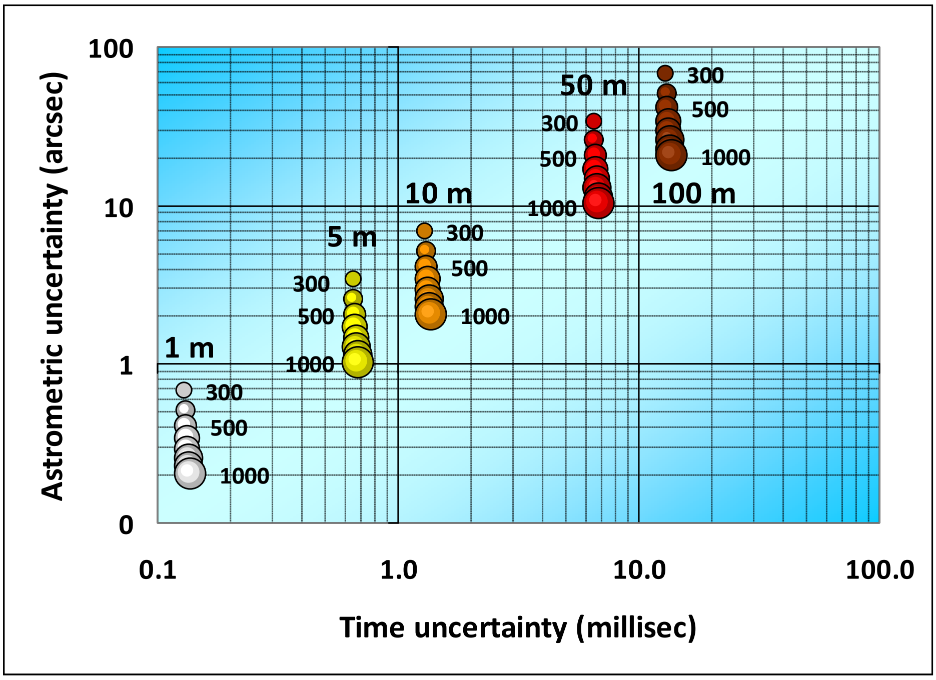

Figure 10 – A comparison of the required accuracy for astrometry and time tag to reach the same absolute metric accuracy in target colocation along its orbit. Each point sequence is labelled according to the LEO quote, from 300 to 1000 km. White dots refer to an absolute accuracy of 1 meter in space, yellow dots are for 5 meters, orange points for 10 meters, red dots for a 50 meters and finally brown markers are for a 100 meters absolute uncertainty. Note that required accuracy figures for time tag of observations (milliseconds or so) far exceed the standard astrometric performance in the target measurements (arcseconds or so).

An error propagation by differentiating the equation leads to

$$\frac{3}{2}\frac{da}{a} = \frac{dP}{P} = \frac{d\tau}{\tau} + \frac{dS}{S}, \tag{17}$$

where we also linked period (P) with the mean orbital distance (a) via the Kepler's Third Law. One sees from the r.h. side of the equation that both time and astrometric uncertainty contribute with nominally the same weight to the orbit definition. However, as operational constraints set in general, $d\tau/\tau >> dS/S$, orbit accuracy is in fact limited by the inherent uncertainty in the clock than by positional mark up.

For example, suppose to take a 5 sec exposure of a LEO satellite crossing at a 400 km altitude and moving at a rate $\omega_{sat} \approx 1^{\circ}$ s^{-1}. Along the exposure, the object spans an arclet of 5°. If our clock accuracy reaches 0.001 sec rms and we perform astrometry at the best of, say, 0.2 arcsec rms, then eq. (17) leads to a relative uncertainty on P of the order of one part in 5000, or just one second for an expected period of 92 min, as

$$\frac{dP}{P} \approx \frac{0.001}{5} + \frac{0.2}{3600 \times 5} = 2 \cdot 10^{-4} + 10^{-5}. \tag{18}$$

Note, from the equation, that the error budget is largely dominated the time-tag term, one order of magnitude larger than the relative astrometric uncertainty. Again, by recalling eq. (17), this case leads as well to a relative uncertainty of one part in 7000 on the orbit semi-major axis a, that is about one kilometer for our example.

At the current technical capabilities of optical sensors, this unbalanced condition between the two error sources is always the prevailing one at LEO orbital regimes. However, as $\omega_{sat} \approx dS/d\tau$, for the previously assumed accuracy figures, we have that clock tuning and astrometry performance may equally contribute to the error budget when $\omega_{sat} \leq 0.2/(3600 \times 0.01) \sim 0.006^{\circ}$ s^{-1}, which is actually the case for MEO (prograde) orbits at 20,000 km or higher (for instance the GPS satellites, see eq. 2). Notably enough, this condition is never met, on the contrary, by objects in retrograde orbit, whatever their altitude.

4 Results and discussion

The intervening importance of the space traffic management at Low-Earth orbital regimes is nowadays a mandatory requirement to keep our access to space in the wake of a sustainable growth. Aside the full range of actions foreseen or yet set in place at international level by private and institutional stakeholders, we have focused here on the plain (unavoidable) step aimed at achieving and maintaining an up-to-date census of the existing population of satellites and demised/uncooperant debris by orbital tracking from radar and optical ground stations.

As for the optical tracking, we did emphasize, throughout our discussion, that any comparison with the standard astronomical context might be greatly misleading as LEO situational awareness demands a somewhat “unconventional” approach both in terms of telescope technical capabilities and observing strategy.

In particular, we have shown in Sec. 2 that fast-trailing objects in LEO, transiting below 1000 km altitudes, far more resemble the case of a liner aircraft crossing the sky at some 0.5°-1.5° s^{-1} angular rates rather than any asteroid quietly wandering at the Mars distance. With SST observations we therefore have to effectively deal with angular rates over two orders of magnitude larger than the sideral rate of astronomical tracking (see **Tab. 1** and **Fig. 1**).

Though extremely short, the crossing time of LEO satellites over a ground station (typically well less than 10 minutes) nonetheless spans a non-negligible fraction (some 10-15%) of the entire orbit. If good positional measurements can be collected along the narrow visibility window, then a good chance exists, in principle, to confidently assess the orbit for any observed target nearly in real time. Timeliness is a must in this regard, as at LEO quotes orbital parameters quickly evolve under the influence of Earth oblateness and other gravitational perturbations.

Figure 11 is an illustrative example in this sense. It shows the epoch distribution of the two-line elements (TLE) for the whole NORAD/Celestrack[5] database of orbiting objects within a period of 110 min (some 15,000 entries in the plot). One sees from the figure that for most of the LEO population the orbit is refreshed (at least) on a daily basis.

A recognized difficulty when tracking LEO satellites optically is the critical constraint due to Sun illumination. The geometrical circumstances that allow an orbiting object to be sunlit against the dark sky when observed from the ground are explored in Sec. 3 leading to a parametric relationship (cf. eq. 8 and **Fig. 6**) of the shadowing conditions with changing the satellite quote.

[5] See https://celestrak.org/

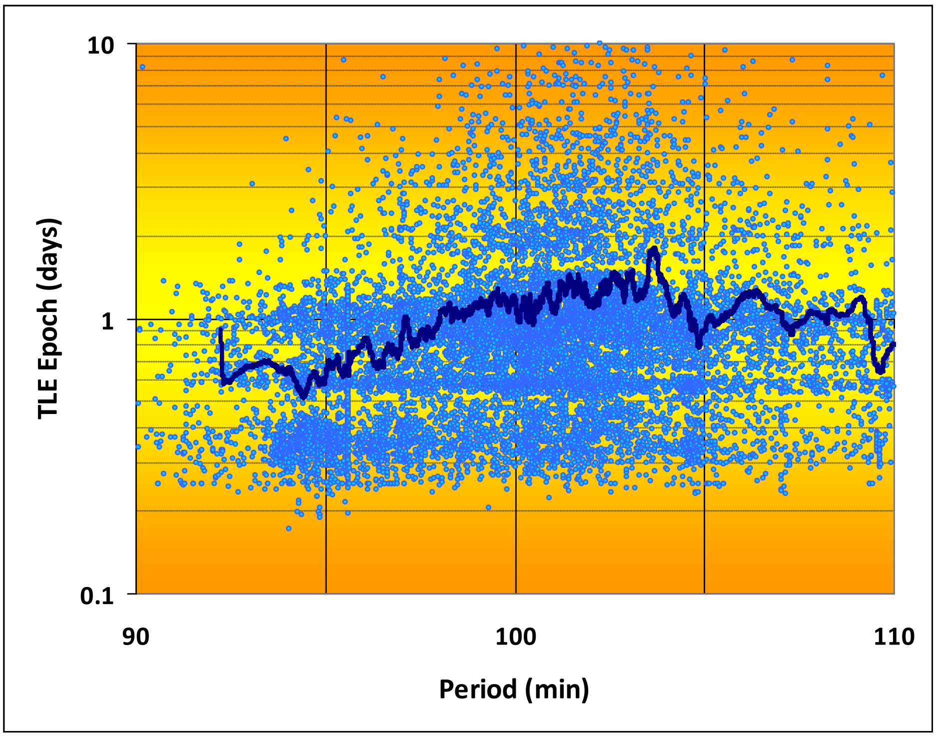

Figure 11 – The epoch distribution of an illustrative sample of the NORAD/Celestrak TLE database for the LEO population according to the orbital period in minutes. About 15,000 objects are displayed in the plot, within a 110 min period. Superposed (black curve) is a moving average over 200 points. Note that for most of the objects the orbit is refreshed once (or even twice) a day.

At intermediate latitudes, we have shown that objects below 1000 km can be under Sun's illumination in at least half the sky vault (face West at sunset or face East at dawn) within a time window of 100±12 minutes after the nautical twilight instant at the sunset (or symmetrically before the dawn). This optimal visibility window further shrinks to some 70±2 min when observing from the Equator.

A comparative assessment of the "surveying" vs. "tracking" strategy to reach a better inventory of the orbiting population at a certain epoch has been discussed in Sec. 3.2-3.4. In fact, two conflicting arguments, one of photometric nature, the other dealing with astrometry, have to be tackled to properly tune-up our observing strategy.

From one hand, the "stare and wait" approach inherent to surveying, is hampered by the fact that the signal of a fast-moving target spreads across many pixels of the CCD/CMOS detector. Somewhat counter-intuitively, this makes our telescope less sensitive with increasing exposure time as target is detected at increasingly poorer S/N ratio [$(S/N)_{sat} \propto \tau_{\rm exp}^{-1/2}$ according to eq. 13] against the sky noise.

On the other hand, by docking the target and stacking its signal on the same pixel(s), like in any active tracking strategy, we certainly improve the object detection [as, now, $(S/N)_{sat} \propto \tau_{\rm exp}^{1/2}$] but we might fatally yield on the side of positional accuracy. Actually, any larger exposure time makes an increasing fraction of surrounding stars to trail away and overspill the FOV border of our imagery (see **Fig. 8**). Target positional information will rely, at the end, on a lower number of reference stars ($n_* \propto \tau_{\rm exp}^{-1}$), which provide the local astrometric grid for our measurements so that, by recalling eq. (15), $\sigma_{sat} \propto n_*^{-1/2} \propto \tau_{\rm exp}^{1/2}$.

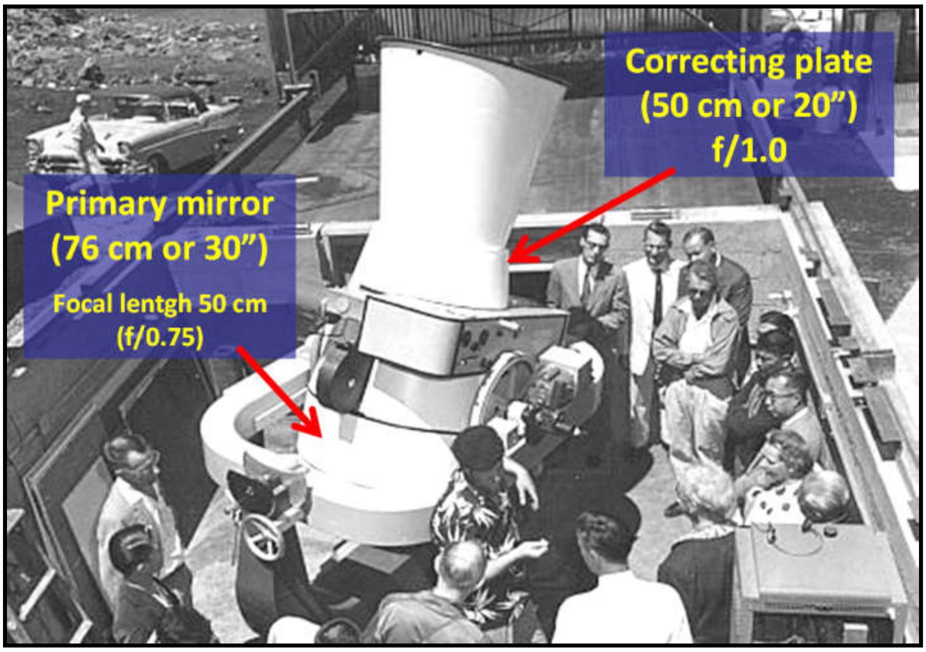

Figure 12 – The SAO Baker-Nunn camera for satellite tracking, one out of a total of 17 worldwide stations, was dedicated on Aug 2, 1958 at the Haleakala Hawaiian observatory. The main optical features of this telescope are marked in the figure. In particular, we recognize the 76 cm primary mirror and the 50 cm correcting plate, which offered a relative aperture of f/1 for the whole instrument. The original image is courtesy of Prof. Walter Steiger[6].

No matter, and whatever our observing strategy, the mandatory requirement is that target detection always should be reached with the *minimum* exposure time, as discussed in Sec. 3.3. In addition, both for surveying and tracking, a FOV as wide as possible is always a welcomed plus for our telescope. A larger FOV will make our survey observations more efficient and, in case of active tracking, will provide us with a larger number of reference stars in the target field, useful for astrometry. A wise trade-off with exposure time has to be considered however as, the smaller the FOV, the deeper the reached magnitude limit to sample a suitable number of stars. **Table 4** and **Fig. 9** provide some useful figures, based on the Bahcall & Soneira (1980) model of apparent stellar density across the Milky Way.

The technical constraints to reach a wide FOV for optical telescopes have been discussed in Sec. 3.2 showing that, in general, this would call for a short focal length. Assuming our telescope to be equipped with a big (Medium Format) monolithic CMOS detector 60 mm on a side, then eq. (10) indicates that a focal length of $F = (3.4 / FOV^o)$ meters is required, independently from the telescope aperture. As shown in **Fig. 7**, this means that for metric apertures, extremely challenging f-numbers should be reached, with a more elaborated (and costly) primary mirror to be always coupled with a train of aberration correctors.

The Baker-Nunn telescope network (see **Fig. 12**) of the 60's (Brandenberger, 1962; Hayes 1968; Massevitch & Losinsky, 1970) still remains an unarrived milestone in this sense. The 17 telescopes of the planetary network (12 operated by the Smithsonian Astrophysical Observatory, SAO and 5 operated by the US Air Force) borrowed a Schmidt optical design, sporting a 30" (76 cm) primary mirror with a 20" (50 cm) focal length. The "curved" FOV was

[6] The unannotated image is available at https://about.ifa.hawaii.edu/origins-of-astronomy-in-hawaii

recovered by a big (20" or 50 cm) correcting plate in front of the primary mirror, as marked in **Fig. 12**, that correspondingly reduced the entrance pupil, and eventually led the telescope relative aperture to f/1 allowing to adjust a 5^{o}x5^{o} FOV on a Kodak photographic film[7] with a remarkable platescale of some 400 arcsec/mm, according to eq. (9).

The pioneering SST experiments of late 50's and early 60's, promptly made clear that a unique attention had to be devised to accurately tagging time of the optical observations. This is the obvious consequence of the fact that, by orbiting at some 8 km/sec, a LEO satellite travels a distance of about 10 meters in just 0.001 sec. As we have been discussing in Sec. 3.5, in order to equate the standard astrometric performance, that locates a LEO target within a few meters transverse to its motion vector, a clock accuracy should be required on a millisecond timescale along the motion direction (see **Fig. 10**).

This so challenging timing accuracy was originally reached even for the Baker-Nunn stations via sophisticated stroboscopic methods by an electro-mechanical Norman crystal clock, and the nominal performance then even further improved to some 0.1 millisec (Hayes 1968) with the so-called EECo electronic clocks introduced since 1965.

It is clear, however, that at these accuracy figures, the ultimate constraint on time tag actually resides in the shutter properties, usually far slower especially for mechanical shutters as in the 60's devices. Things are only marginally better nowadays as exposure in CMOS chips can be handled electronically on timescales of 10^{-5} sec per pixel row. In any case, as exposure and chip read-out may proceed sequentially by rows (the so-called "rolling shutter" effect, see e.g. Liang, Peng & Chen, 2008), then a relevant (yet recoverable) drift, in the order of few 10^{-2} sec, in the nominal time tag of the shot across the CMOS frame should be carefully considered. Allover, the millisec performance is still a challenging threshold when managing 10-30 Mpx imagery and this is why, when discussing eq. (17), the time-tag term still prevails in the error budget for orbit determination of objects up to altitudes of some 20,000 km, especially to constrain the orbital period and mean geocentric distance.

5 The Three Golden Rules for optimum optical tracking of LEO objects

For better convenience of the reader, we would like to end our brief excursus with an essential excerpt of the "Three Golden Rules" for an optimum assessment of the LEO traffic.

1. Accurate time management is mandatory, all the way, to set the ultimate quality of our observations. A millisec accuracy must be the reference "quantum" for our clock and a CMOS technology should be preferred for our detector, by relying on electronic (not mechanical) shutter and, in case, on a cautious account of the "rolling shutter" effect, to properly deal with the sharp time constraints of our imagery.
2. Exposure time should be kept as short as possible, ideally approaching the pixel latency time, as from eq. (12), though large enough to reveal an adequate number (a few dozen or so) of reference stars in the field. Equation (11) can be taken as a guideline. A trailing target, as in a longer exposure, may sometimes ease the identification but this always happens at cost of a poorer S/N and a correspondingly shallower detection threshold. Whenever possible, a blinking procedure among

[7] In fact, a 5^{o}x30^{o} FOV was sampled along the observing batch by shifting the film stripe. See https://bollerandchivens.com/?p=561 for a detailed description of this technique.

short sequential frames should be pursued, instead, to safely assess the astrometrical properties of (nearly) point-source targets. Attention should be paid, in case of active tracking, to avoid field overspilling of trailing stars.

3. For mid-latitude ground sensors, a maximum observing proficiency is achieved within the first 100±12 minutes following/preceding the nautical twilight, respectively at the sunset or before the sunrise. This window will assure the whole LEO population orbiting up to 1000 km to be sunlit in at least half the sky vault.

References:

– Aglietti, G. S. and 16 colleagues 2020. The active space debris removal mission RemoveDebris. Part 2: In orbit operations. Acta Astronautica 168, 310–322. doi:10.1016/j.actaastro.2019.09.001

– Allen, C.W. 1973. Astrophysical quantities. London: University of London, Athlone Press, 3rd ed., p. 243.

– Bahcall, J. N., Soneira, R. M. 1980. Star counts as an indicator of galactic structure and quasar evolution. The Astrophysical Journal 238, L17–L20. doi:10.1086/183248

– Brandenberger, A. J. 1962. The Use of Baker-Nunn Cameras for Tracking of Artificial Earth Satellites. Photogrammetric Engineering & Remote Sensing Journal (PE&RS), ASPRS Soc., Nov. issue, 727. Also available in electronic form at: https://www.asprs.org/wp-content/uploads/pers/1962journal/nov/1962_nov_727-735.pdf

– Buzzoni, A., Altavilla, G., Galleti, S. 2016. Optical tracking of deep-space spacecraft in Halo L2 orbits and beyond: The Gaia mission as a pilot case. Advances in Space Research 57, 1515–1527. doi:10.1016/j.asr.2016.01.003

– Buzzoni, A. and 7 colleagues 2019. Physical characterization of the deep-space debris WT1190F: A testbed for advanced SSA techniques. Advances in Space Research 63, 371–393. doi:10.1016/j.asr.2018.07.025

– Buzzoni, A., Guichard, J., Altavilla, G., Figer, A., Alessi, E. M., Tommei, G. 2019. Toward a Physical Characterization of the Soviet/Russian Constellation of Molniya Satellites. First International Orbital Debris Conference, paper no. 6067. Available in electronic form at: https://www.hou.usra.edu/meetings/orbitaldebris2019/orbital2019paper/pdf/6067.pdf

– Cooper, J., Juvan-Beaulieu, I., Wise, A. 2019. Scientific CMOS Optical Detectors for Orbital Debris Observations. First International Orbital Debris Conference, paper no. 6207. Available in electronic form at https://www.hou.usra.edu/meetings/orbitaldebris2019/orbital2019paper/pdf/6207.pdf

– Emanuelli, M., Federico, G., Loughman, J., Prasad, D., Chow, T., Rathnasabapathy, M. 2014. Conceptualizing an economically, legally, and politically viable active debris removal option. Acta Astronautica 104, 197–205. doi:10.1016/j.actaastro.2014.07.035

– Gaia Collaboration and 455 colleagues 2023. Gaia Data Release 3. Summary of the content and survey properties. Astronomy and Astrophysics 674, 1-22. doi:10.1051/0004-6361/202243940

- Jankovic, M., Yüksel, M., Babr, M. M., Letizia, F., Braun, V. 2020. Space debris ontology for ADR capture methods selection. Acta Astronautica 173, 56–68. doi:10.1016/j.actaastro.2020.03.047
- Hainaut, O.R., Williams, A.P. 2020. Impact of satellite constellations on astronomical observations with ESO telescopes in the visible and infrared domains. Astronomy and Astrophysics 636, 121-132. doi:10.1051/0004-6361/202037501
- Hayes, N. E. 1968. Trackers of the skies. A history of the Smithsonian satellite-tracking program. Howard A. Doyle Publishing, Cambridge MA 02139.
- Hejduk, M., Cowardin, H., Stansbery, E. 2012. Satellite material type and phase function determination in support of orbital debris size estimation. Advanced Maui Optical and Space Surveillance Technologies Conference (AMOS), Ed.: S. Ryan, The Maui Economic Development Board, id. 14.
- Høg, E. and 8 colleagues 2000. The Tycho-2 catalogue of the 2.5 million brightest stars. Astronomy and Astrophysics 355, L27–L30.
- Kessler, D. J., Cour-Palais, B. G. 1978. Collision frequency of artificial satellites: The creation of a debris belt. Journal of Geophysical Research 83, 2637–2646. doi:10.1029/JA083iA06p02637
- King-Hele, D. 1983. Observing Earth Satellites. MacMillan Pub., London. ISBN: 0333330412
- Klinkrad, H. 2006. Space Debris: Model and Risk Analysis. Springer Verlag, Berlin
- Klinkrad, H., Tremayne-Smith, R., Alby, F., Alwes, D. 2008. Europe's eyes on the skies. ESA Bulletin no. 133. Available in electronic form at https://www.esa.int/esapub/bulletin/bulletin133/bul133f_klinkrad.pdf
- Kulu, E. 2023. Small Launchers: 2023 Industry Survey and Market Analysis. 74th International Astronautical Congress (IAC 2023). IAC-23-D2.IP.7
- Lasker, B. M. and 25 colleagues 2008. The Second-Generation Guide Star Catalog: Description and Properties. The Astronomical Journal 136, 735–766. doi:10.1088/0004-6256/136/2/735
- Lawler, S.M., Boley, A.C., Rein, H. 2022. Visibility Predictions for Near-future Satellite Megaconstellations: Latitudes near 50^{o} Will Experience the Worst Light Pollution. The Astronomical Journal 163, 21-34. doi:10.3847/1538-3881/ac341b
- Lawrence, A. and 10 colleagues 2022. The case for space environmentalism. Nature Astronomy 6, 428–435. doi:10.1038/s41550-022-01655-6
- Liang, Ch., Peng, Y., Chen, H. 2008. Analysis and Compensation of Rolling Shutter Effect. IEEE transactions on image processing 17(8), 1323, doi:10.1109/tip.2008.925384
- Lindegren, L. and 89 colleagues 2018. Gaia Data Release 2. The astrometric solution. Astronomy and Astrophysics 616, 2-26. doi:10.1051/0004-6361/201832727
- Liou, J.-C. 2011. An active debris removal parametric study for LEO environment remediation. Advances in Space Research 47, 1865–1876. doi:10.1016/j.asr.2011.02.003
- Macko, S. 1962. Satellite Tracking. Rider Pub. Inc. New York. ISBN: 1124016228
- Massevitch, A. G. , Losinsky, A. M., 1970. Photographic Tracking of Artificial Satellites. Space Science Rev, 11, 308

- McKnight, D. and 18 colleagues 2021. Identifying the 50 statistically-most-concerning derelict objects in LEO. Acta Astronautica 181, 282–291. doi:10.1016/j.actaastro.2021.01.021
- Meeus, J. 1991. Astronomical Algorithms, Willmann-Bell Inc., Richmond VI, USA. ISBN: 0943396352
- Miller, G. D. 2021. Deterrence by Debris: The Downside to Cleaning up Space. Space Policy 58, id 101447. doi:10.1016/j.spacepol.2021.101447
- Montenbruck, O., Pfleger, Th. 1984. Astronomy on the Personal Computer. 2nd Ed., Springer-Verlag, New York. ISBN: 0387577009
- Newman, C. J., Williamson, M. 2018. Space Sustainability: Reframing the Debate. Space Policy 46, 30–37. doi:10.1016/j.spacepol.2018.03.001
- Niels Bohr Institute U. o. C. Inst. Of Astronomy C., UK, Real Inst. Y Obs. De la Armada en San Fernando, 2014, Carlsberg Meridian Catalog Number 15
- Pardini, C., Anselmo, L. 2021. Evaluating the impact of space activities in low earth orbit. Acta Astronautica 184, 11–22. doi:10.1016/j.actaastro.2021.03.030
- Peter, N. 2006. The changing geopolitics of space activities. Space Policy 22, 100–109. doi:10.1016/j.spacepol.2006.02.007
- Peterson, G. 2002. Maneuver optimization for collision avoidance of LEO objects. 34th COSPAR Scientific Assembly.
- Petroni, G., Bianchi, D.G. 2016. New patterns of space policy in the post-Cold War world. Space Policy 37, 12–19. doi:10.1016/j.spacepol.2016.10.002
- Roeser, S., Demleitner, M., Schilbach, E. 2010. The PPMXL Catalog of Positions and Proper Motions on the ICRS. Combining USNO-B1.0 and the Two Micron All Sky Survey (2MASS). The Astronomical Journal 139, 2440–2447. doi:10.1088/0004-6256/139/6/2440
- Santoni, F., Piergentili, F. 2013. Results of observation campaigns for satellite orbital and attitude motion determination. 6th European Conference on Space Debris. Ed. L. Ouwehand. ESA SP-723, ISBN 978-92-9221-287-2, id. 164
- Schildknecht, T., Vannanti, A., Krag, H., Erd, C. 2009. Reflectance spectra of space debris in GEO. Advanced Maui Optical and Space Surveillance Technologies Conference. Ed.: S. Ryan, The Maui Economic Development Board., id. E24
- Schildknecht, T. and 6 colleagues 2013. Improved Space Object Observation Techniques Using CMOS Detectors. 6th European Conference on Space Debris 723. Available in electronic form at: https://conference.sdo.esoc.esa.int/proceedings/sdc6/paper/190/SDC6-paper190.pdf
- Space Investment Quarterly, Q3. 2017. Space Angels Pub., also available in electronic form from the URL: https://forum.nasaspaceflight.com/index.php?action=dlattach;topic= 40437.0;attach=1457378
- Stokes, H. and 16 colleagues 2019. Evolution of ISO's Space Debris Mitigation Standards. First International Orbital Debris Conference, paper no. 6053. Available in electronic form at: https://www.hou.usra.edu/meetings/orbitaldebris2019/orbital2019paper/pdf/6053.pdf

- Veis, G. 1963. Optical Tracking of Artificial Satellites. Space Science Reviews 2, 250–296. doi:10.1007/BF00216781
- Zacharias, N. and 16 colleagues 2015. The First U.S. Naval Observatory Robotic Astrometric Telescope Catalog. The Astronomical Journal 150, 101-113. doi:10.1088/0004-6256/150/4/101
- Zacharias, N., Finch, C., Frouard, J. 2017. UCAC5: New Proper Motions Using Gaia DR1. The Astronomical Journal 153, 166-174. doi:10.3847/1538-3881/aa6196